*American Mineralogist, Volume 93, pages 210–216, 2008*

# Synthesis and characterization of low-$OH^-$ fluor-chlorapatite: A single-crystal XRD and NMR spectroscopic study

**Francis M. McCubbin,[1,*] Harris E. Mason,[1] Hyunsoo Park,[2] Brian L. Phillips,[1] John B. Parise,[1,2] Hanna Nekvasil,[1] and Donald H. Lindsley[1]**

[1]Department of Geosciences, Stony Brook University, Stony Brook, New York 11794-2100, U.S.A.
[2]Department of Chemistry, Stony Brook University, Stony Brook, New York 11794-3400, U.S.A.

## Abstract

Low-OH apatite of the compositional range $Ca_{4.99–5.06}(PO_4)_{2.98–3.00}F_{0.51–0.48}Cl_{0.38–0.36}OH_{0.14–0.12}$ was synthesized and characterized structurally by synchrotron-based single-crystal X-ray diffraction (XRD), and multiple nuclear magnetic resonance (NMR) spectroscopic techniques. The average structure is hexagonal with space group $P6_3/m$. The presence of scattering in the single-crystal diffraction data set, which is incommensurate within the average hexagonal structure, suggests the presence of localized short-range monoclinic domains. Complex lineshapes in the $^{31}P$ and $^{19}F$ MAS NMR spectra are also consistent with the presence of an incommensurate phase. No evidence was detected for splitting of the Ca2 site into two distinct sites (as had been previously reported for hexagonal ternary apatites). Structure refinement and $^{19}F\{^{35}Cl\}$ TRAPDOR NMR experiments verified intercolumnal neighboring of F and Cl atoms (inter-column distance of 2.62 Å) within this low-$OH^-$ apatite suggesting that long-range neighboring of F and Cl within the apatite anion channels is feasible.

**Keywords:** Apatite, NMR spectroscopy, single-crystal XRD, Mars, Moon, PGE, synthesis

## Introduction

The mineral apatite is of importance to a wide variety of fields, from earth science to life science, material science, and planetary science (e.g., Hughes and Rakovan 2002). It is the major source of phosphorus on Earth, and its uses range from fertilizers to detergents to insecticides. It is the main constituent of human bone and plays an important part in regulating metabolic functions in the body. Apatite is found in sedimentary, igneous, and metamorphic rocks, and it is an important sink of rare earth elements, which are of primary importance for petrogenetic studies. Also, its ability to accommodate the radioisotopes used for age determinations makes it of major importance to geochronological studies of rocks.

Geologically occurring apatite, most commonly $Ca_5(PO_4)_3(F,Cl,OH)$, generally has either a hexagonal structure with space group $P6_3/m$, or a monoclinic structure with space group $P2_1/b$. Apatite is represented by the structural formula $A[1]_2A[2]_3(BO_4)_3X$ [adopted from White and Dong (2003)] where A[1] and [2] represent the Ca sites, B the phosphorus site, and X the typically monovalent anion site. The X site in apatite provides a basis for solid solution with three primary end-member components, fluorapatite $[Ca_5(PO_4)_3F]$, chlorapatite $[Ca_5(PO_4)_3Cl]$, and hydroxylapatite $[Ca_5(PO_4)_3OH]$. The structures of these end-members have been well studied (see summary of Hughes et al. 1989). The atomic arrangements of the three apatite end-members differ principally in the positions of $F^-$, $Cl^-$, and $OH^-$ in the [00z] anion positions. Binary solid solutions of either $F^-$ and $OH^-$ or $Cl^-$ and $OH^-$ are common (Tacker and Stormer 1989), although not much is known regarding $F^-$ and $Cl^-$ binary solutions. Ternary solution of all three X-site anions in apatite does occur (e.g., Hughes et al. 1990; Piccoli and Candela 2002), however, ternary solution requires that the [00z] columns accommodate a combination of the three different anions. This accommodation requires a structural response because of interactions among the column anions (Hughes and Rakovan 2002). Based on a variety of studies it was concluded that miscibility of $F^-$, $Cl^-$, and $OH^-$ in hexagonal ternary apatite results from a Markovian sequence of anions in which the occupant of a given position is dependent on the occupant of the adjacent position (Hughes and Rakovan 2002). This accommodates the three anions in a single column without vacancies. The shift in anionic positions induced by anion mixing also affects the cation positions. It has been proposed that anionic mixing among the three X-site anions is coupled by a splitting of the single Ca2 site into two sites (Sudarsanan and Young 1969). Such structural adjustments have been summarized by Hughes et al. (1990). These workers, however, also reported a monoclinic variant of the ternary apatite structure in which a reduction in symmetry results from ordering in the anionic columns. As acknowledged by Hughes and Rakovan (2002) however, column anion interactions may inhibit binary solution of fluorapatite and chlorapatite because the position of the fluorine atoms, [00¼] and [00¾], deviates from that of chlorine by about 1.2 Å because of differences in ionic radii (Hughes and Rakovan 2002). In fact, Hughes et al. (1990) suggested that in natural apatites $OH^-$ may be an essential component in stabilizing fluorapatite-chlorapatite solid solutions.

There is some natural evidence for the stability of $OH^-$-poor, fluor-chlorapatites. Boudreau et al. (1995) compiled extensive data on channel anion compositions of natural apatites from various layered intrusions. This compilation showed the pre-

* E-mail: fmccubbi@ic.sunysb.edu

dominance of $OH^-$-rich apatite in natural layered intrusions. However, Bushveld (below the PGE zones) contains Cl-rich, $OH^-$-poor apatite. Additionally, Martian meteorites, specifically Chassigny and Nakhla, contain apatite with reported analyses indicating low $OH^-$ contents (e.g., Bunch and Reid 1975; McCubbin et al. 2006, 2007). Lastly, evaluation of lunar apatite data from Apollo 14 basalts (Taylor et al. 2004) and Apollo 14 soils (Jolliff et al. 1993) also shows the presence of fluor-chlorapatites with computed low $OH^-$ contents.

There is an apparent inconsistency between the structural considerations listed above and the reports of natural $OH^-$-poor apatites. This questions the reliability of either the inferred structural characteristics of apatite or the reported analytical data. This work is aimed at evaluating this inconsistency by determining whether or not there is a previously unreported structural adjustment in $OH^-$-poor apatite that facilitates the existence of long-range $F^-$–$Cl^-$ neighboring in apatite.

## Analytical/experimental methods

### Apatite synthesis

The composition of synthetic apatite selected for use in this study is $Ca_5(PO_4)_3(F_{0.5}Cl_{0.5})$. This composition was achieved by mixing powdered $Ca_3(PO_4)_2$, $CaF_2$, and $CaCl_2$. Due to the hygroscopic nature of $CaCl_2$, steps were taken to limit, as much as possible, the amount of $H_2O$ in the starting material. First, the mix was dried in a platinum crucible overnight at 500 °C to drive off absorbed $H_2O$. Next, the powder was loaded into a platinum capsule and inserted in a silica glass tube, from which a capillary was pulled. The tube was then attached to a vacuum pump and placed in a pot furnace at 800 °C to drive off structurally bound $H_2O$. The tube was left under a pumping vacuum for 24 h at 800 °C to maximize $H_2O$ loss. Subsequently, the evacuated silica glass tube was sealed and placed in a horizontal tube furnace at 900 °C. Synthesis of apatite in vacuum was done to avoid the complications of $O^{2-}$ substitution into the apatite X site (Pan and Fleet 2002). The synthesis duration was 14 days. This period was found to be sufficient for growing crystals large enough for single-crystal diffraction at a third generation synchrotron source.

### EPMA analysis

Electron microprobe analyses (EPMA) of the synthetic apatite grains were performed using a Cameca Camebax electron microprobe equipped with four wavelength dispersive spectrometers, one of which was equipped with an OV-60 detector crystal necessary for obtaining accurate fluorine analyses. An accelerating voltage of 15 kV and a nominal beam current of 10 nA were used during all analyses. Anorthite, apatite, barium apatite, and magnesium fluoride were used as standards for Ca, P, Cl, and F, respectively. The largest possible raster size was used to minimize unknown analytical problems that may occur during highly focused electron beam analyses. To avoid apparent anisotropic diffusion of fluorine and chlorine during EPMA analyses down the **c**-axis of apatite (Stormer et al. 1993), care was taken to measure down the **a**-axis whenever possible. Hydroxyl was not directly measured in this study; it was calculated assuming that only fluorine, chlorine, and hydroxyl populate the apatite X site, and that the X site sums to one when normalized to 13 anions.

### X-ray powder diffraction

X-ray powder diffraction analysis was performed on a Scintag PAD X diffractometer using Cu$K\alpha$ radiation. The synthesized powder was prepared as a smear mount on a glass slide and analyzed at 40 kV and 25 mA using a continuous scanning procedure with a scan rate of 0.75 °2θ/min over the range 5–90 °2θ. The resulting X-ray pattern was used to indicate sample purity and completeness of reaction.

### Single-crystal X-ray diffraction

Synchrotron X-ray data were collected to obtain a diffraction signal with sufficient peak-to-background discrimination to aid in the assignment of a correct symmetry (monoclinic vs. hexagonal) as well as to obtain precise positions of the anions along the *c* axis. Data collection and structure determination were carried out at 15-ID ChemMatCARS beamline at the Advanced Photon Source, Argonne National Laboratory. A small crystal of $0.03 \times 0.03 \times 0.03$ mm$^3$ in dimension was selected and mounted on a glass fiber with Paratone oil. The data were collected at 100 K with wavelength of 0.4959(2) Å, exposure time of 1 s per frame, and a detector distance of 5.0 cm. A randomly oriented region of reciprocal space was examined to a resolution of 0.75 Å. Two major sections of frames were collected with a step size of 0.30° in ω and φ. The raw intensity data were collected and integrated with software packages SMART (2001) and SAINT (2002), then an empirical absorption correction was applied using SADABS (Sheldrick 2001). The final unit-cell parameters were determined from 1024 strong reflections after integration. The crystal structures were solved via the direct method and refined with the program SHELXTL (Sheldrick 2000) assuming anisotropic displacement parameters for all atoms except the hydroxyl O atom. Calcium and phosphorus atoms were located first, and the remaining atoms (O, Cl, F) were found from subsequent Fourier difference map synthesis.

### NMR spectroscopy

$^{31}$P Single-pulse (SP) magic angle spinning (MAS) nuclear magnetic resonance (NMR), $^{19}$F SP MAS NMR, $^{35}$Cl SP MAS NMR, $^{31}$P{$^1$H} cross polarization (CP)/MAS, $^{31}$P{$^{19}$F} CP/MAS NMR, and $^{19}$F{$^{35}$Cl} transfer of population double resonance (TRAPDOR) NMR spectra of the synthetic apatite were collected on a 500 MHz Varian Infinity Plus spectrometer at operating frequencies of 499.78, 470.21, 204.32, and 48.97 MHz for $^1$H, $^{19}$F, $^{31}$P, and $^{35}$Cl, respectively. For all experiments the samples were contained within 3.2 mm (o.d.) zirconium oxide rotors.

$^{31}$P SP MAS NMR spectra were collected at a spinning rate of 10 kHz with a 4 µs pulse and a 120 s pulse delay to ensure full spin lattice relaxation. $^{31}$P{$^1$H} and $^{31}$P{$^{19}$F} CP/MAS NMR spectra were collected using a radio frequency (rf) amplitude ramp for a variety of contact times and at a spinning rate of 5 kHz. All $^{31}$P spectra were referenced to 85% phosphoric acid using hydroxylapatite as a secondary reference set to +2.65 ppm. $^{35}$Cl SP MAS NMR spectra were collected at a spinning rate of 14 kHz using an excitation pulse of 1.5 µs and were referenced with respect to a 1 *M* NaCl solution using reagent-grade KCl as an external reference set at +3.07 ppm (Bryce and Sward 2006). $^{19}$F SP MAS NMR were collected at a spinning rate of 24 kHz with 5 µs excitation pulses on a 3.2 mm Varian/Chemagnetics probe configured to give a low $^{19}$F background signal. No $^{19}$F signal was observed after several days of acquisition on an empty rotor. Using the quadrupolar frequency ($\nu_Q$) for $^{35}$Cl in the synthetic apatite obtained from the $^{35}$Cl SP MAS spectrum, and a spinning rate of $\nu_{rot}$ = 16 kHz, the rf amplitude applied to the $^{35}$Cl spins during the TRAPDOR experiment ($\nu_1$) was set to 83.3 kHz so that the adiabaticity parameter ($\alpha'$), calculated as $\alpha' = \nu_1^2/\nu_{rot}\nu_Q$, would be approximately greater than one (Grey and Vega 1995). The $^{19}$F observed spectra were referenced with respect to $CFCl_3$. The $^1$H SP MAS NMR spectra were obtained on a 400 MHz Varian Inova operating at 399.76 MHz using a Chemagnetics probe assembly configured for 4 mm (o.d.) rotors and modified to yield very low $^1$H background signal. The probe assembly with empty rotors yields a broad $^1$H background signal that is much lower than that from the sample and which was not removed from the spectra. A spinning rate of 15 kHz and a 90° pulse width of 3.5 µs were used. The $^1$H MAS NMR spectra were referenced with respect to tetramethylsilane (TMS) by setting the hydroxyl resonance in reagent-grade hydroxylapatite to +0.2 ppm. $^{31}$P{$^1$H} 2-dimensional (2-d) Heteronuclear Correlation (HetCor) NMR spectra were collected on the 400 MHz spectrometer at frequencies of 162.82 and 399.76 MHz for $^{31}$P and $^1$H, respectively. A total of 128 hypercomplex points in $t_1$ were collected with a 20 µs increment, corresponding to a 50 kHz F1 spectral window. A spinning rate of 10 kHz was used and spectra collected at contact times ranging from 1.0 to 15.0 ms using a linear ramp of the $^1$H field to optimize signal intensity. Data were processed with standard linear prediction methods to complete the signal in $t_1$.

## Results

### Apatite synthesis

The above synthesis technique produced chemically homogenous apatite crystals with compositions in the range $Ca_{4.99–5.06}(PO_4)_{2.98–3.00}F_{0.51–0.48}Cl_{0.38–0.36}OH_{0.14–0.12}$ as determined by electron microprobe analysis (Table 1). Sample purity was tested by X-ray powder diffraction, and no phase impurities were observed within the detection limits of our scan. The crystals ranged in size from about 30–80 µm in their longest dimension with aspect ratios of about 7:1 or less. Noteworthy is the amount of calcu-

lated $OH^-$ content even after the cumbersome drying technique. We believe this calculated $OH^-$ value is real and reflects the extremely hygroscopic nature of $CaCl_2$.

### Single-crystal XRD

The details of the crystal structures are given in Table 2. Atomic coordinates and isotropic displacement parameters are given in Table 3. Anisotropic displacement parameters are given in Table 4. Selected atomic distances are shown in Table 5, and bond angles are given in Table 6. The crystal structure of our synthesized apatite was solved and refined in the hexagonal space group $P6_3/m$. All reflections were used in the refinement of the structural model. Attempts to refine structure models in space group $P2_1/b$, were unsuccessful, because of a lack of data at positions indicative of the lower symmetry.

Fourier difference maps were synthesized with no anions along the **c**-axis and two large residual peaks were observed. The peak corresponding to lower electron density was located on the mirror plane, [0, 0, ¼], and was assigned to F. The peak with higher electron density was located at [0, 0, 0.361] and was assigned to Cl. A residual density peak corresponding to the hydroxyl oxygen could not be found, probably because of the low abundance of $OH^-$ in the sample. When the refinement was carried out using the above anion positions and proper occupancies, Cl atoms lie closer to the mirror plane than the hydroxyl O atoms. When the hydroxyl O was forced to be at [0, 0, 0.203], that is, at the position reported by Hughes et al. (1990), the displacement parameter of the hydroxyl O atom became negative. If the hydroxyl O is placed further away from the mirror plane at [0, 0, 0.085], its displacement parameter becomes more satisfactory. The coordination environment around Ca2 was also examined to aid the determination of the position of the hydroxyl oxygen. With the hydroxyl O at [0, 0, 0.085], the bond valence sum (Brese and O'Keeffe 1991) around Ca2 is calculated to be 1.86, which is slightly smaller than the expected value of 2. If the hydroxyl O is at [0, 0, 0.203], then the bond valence sum around Ca2 becomes 2.00, matching the oxidation state of $Ca^{2+}$. Based on the bond valence calculations, the position reported by Hughes et al. (1990) seems to be a more appropriate choice. At this point it cannot be definitively stated that the reported O(H) position in Table 3 is a new one because the amount of $OH^-$ is too small to locate its position accurately with X-ray diffraction data (equivalent to one H atom). Moreover, its position is especially difficult to locate because of the rather large displacement parameters of F and Cl along the **c**-axis (Table 4). Examination of the Fourier difference maps as well as the anisotropic displacement parameters of the Cl atom did not indicate multiple Cl positions. Therefore, it appears that the Ca2 site was not split into two distinct sites. When the Ca2 position was forced to split into two separate sites, the refinement became unstable with negative displacement parameters. The single-crystal data were

**TABLE 1.** Electron microprobe data of synthesized apatite

| Oxide | Grain 1 | Grain 2 | Grain 3 | Grain 4 | Grain 5 | Grain 5 | Grain 5 |
|---|---|---|---|---|---|---|---|
| CaO | 55.1(4) | 55.4(4) | 55.2(4) | 54.9(4) | 55.3(4) | 54.4(4) | 54.8(4) |
| $P_2O_5$ | 41.6(3) | 41.3(3) | 41.3(3) | 41.3(3) | 41.2(3) | 41.5(3) | 40.9(3) |
| F | 1.89(4) | 1.79(2) | 1.87(2) | 1.81(4) | 1.85(2) | 1.87(2) | 1.84(2) |
| Cl | 2.58(6) | 2.64(6) | 2.62(6) | 2.57(6) | 2.63(6) | 2.49(6) | 2.45(6) |
| –O = F + Cl | 1.38 | 1.35 | 1.38 | 1.34 | 1.37 | 1.35 | 1.33 |
| Total | 99.78 | 99.74 | 99.60 | 99.26 | 99.59 | 98.91 | 98.66 |
| **Structural formulae based on 13 anions** | | | | | | | |
| Ca | 5.02 | 5.06 | 5.05 | 5.03 | 5.06 | 4.99 | 5.05 |
| P | 2.99 | 2.98 | 2.98 | 2.99 | 2.98 | 3.00 | 2.98 |
| F | 0.51 | 0.48 | 0.50 | 0.49 | 0.50 | 0.51 | 0.50 |
| Cl | 0.37 | 0.38 | 0.38 | 0.37 | 0.38 | 0.36 | 0.36 |
| OH* | 0.12 | 0.14 | 0.12 | 0.14 | 0.12 | 0.13 | 0.14 |
| Cation sum | 8.01 | 8.04 | 8.03 | 8.02 | 8.04 | 7.99 | 8.03 |

*Note:* Numbers inside of parentheses correspond to absolute uncertainties in the last reported digit for each measurement.
* OH calculated by assuming F + Cl + OH = 1.

**TABLE 2.** Crystallographic data for F,Cl,OH-apatite

| | |
|---|---|
| Empirical formula* | $Ca_5Cl_{0.4}H_{0.1}F_{0.5}O_{12.1}P_3$ |
| Formula weight (g/mol) | 510.69 |
| Collection *T* (K) | 100(2) |
| Wavelength (Å) | 0.49594 |
| Space group | $P6_3/m$ |
| Unit-cell dimensions (Å) | $a = 9.441(1)$, $c = 6.835(1)$ |
| Volume (Å³) | 527.6 (2) |
| *Z*, calc. density (g/cm³) | 2, 3.214 |
| Absorption coefficient ($mm^{-1}$) | 1.610 |
| F(000) | 506 |
| Crystal size (mm) | 0.03 × 0.03 × 0.03 |
| θ range (°) | 2.71 to 19.37 |
| Index ranges | $-12 \le h \le 12$ $-12 \le k \le 12$ $-9 \le l \le 8$ |
| Total reflections | 7636 |
| Independent reflections | 454 [*R*(int) = 0.070] |
| Completeness to θ (%) | 94.2 |
| Absorption correction | SADABS |
| Max and min transmission | 0.855 and 0.565 |
| Refinement method | Full-matrix least-squares on $F^2$ |
| Data/restraints/parameters | 454/0/44 |
| Goodness-of-fit | 1.122 |
| Final *R* [$I > 2\sigma(I)$] | $R_1 = 0.0245$ $wR_2 = 0.0599$ |
| *R* (all data) | $R_1 = 0.0262$, $wR_2 = 0.0606$ |
| Largest difference peak and hole (e/Å³) | 0.85 and –0.85 |

* Occupancies used for refining anion positions.

**TABLE 3.** Atomic coordinates and isotropic displacement parameters

| | *x* | *y* | *z* | *U* (Å²) |
|---|---|---|---|---|
| Ca1 | 2/3 | 1/3 | 0.00159(9) | 0.00377(18) |
| Ca2 | –0.00483(7) | 0.24902(7) | 1/4 | 0.00676(18) |
| P1 | 0.36958(8) | 0.40062(7) | 1/4 | 0.00156(18) |
| O1 | 0.4860(2) | 0.3313(2) | 1/4 | 0.0044(4) |
| O2 | 0.4654(2) | 0.5889(2) | 1/4 | 0.0076(4) |
| O3 | 0.2593(1) | 0.3455(2) | 0.0695(2) | 0.0112(3) |
| F1 | 0 | 0 | 1/4 | 0.019(2) |
| Cl1 | 0 | 0 | 0.126(2) | 0.029(2) |
| O4 (OH) | 0 | 0 | 0.41(3) | 0.26(8) |

**TABLE 4.** Anisotropic displacement parameters

| Atom | $U_{11}$ | $U_{22}$ | $U_{33}$ | $U_{23}$ | $U_{13}$ | $U_{12}$ |
|---|---|---|---|---|---|---|
| Ca1 | 0.0053(2) | 0.0053(2) | 0.0008(3) | 0 | 0 | 0.00263(11) |
| Ca2 | 0.0025(3) | 0.0120(3) | 0.0021(3) | 0 | 0 | 0.0009(2) |
| P1 | 0.0024(3) | 0.0024(3) | 0.0008(3) | 0 | 0 | 0.0019(2) |
| O1 | 0.0033(8) | 0.0068(9) | 0.0056(9) | 0 | 0 | 0.0044(7) |
| O2 | 0.0069(9) | 0.0026(8) | 0.0132(9) | 0 | 0 | 0.0023(7) |
| O3 | 0.0095(7) | 0.0229(8) | 0.0074(7) | –0.0093(6) | –0.0059(5) | 0.0128(6) |
| F1 | 0.007(3) | 0.007(3) | 0.042(6) | 0 | 0 | 0.0035(16) |
| Cl1 | 0.0022(15) | 0.0022(15) | 0.081(7) | 0 | 0 | 0.0011(7) |

**TABLE 5.** Atomic distances

| Bonds | Distance (Å) | Bonds | Distance (Å) |
|---|---|---|---|
| Ca1-O1 ×3 | 2.400(1) | P1-O1 | 1.535(2) |
| Ca1-O2 ×3 | 2.443(1) | P1-O2 | 1.540(2) |
| Ca1-O3 ×3 | 2.793(2) | P1-O3 ×2 | 1.528(1) |
| Ca2-O2 | 2.339(2) | | |
| Ca2-O3 ×2 | 2.333(1) | | |
| Ca2-O3 ×2 | 2.510(1) | Anion···Anion | |
| Ca2-F1 | 2.3741(7) | F···OH | 2.26 |
| Ca2-Cl1 | 2.520(6) | F···Cl | 2.62 |
| Ca2-OH | 2.60(2) | Cl···OH | 3.05 |

**TABLE 6.** Selected bond angles (°)

| | | | |
|---|---|---|---|
| $O1^{i}$-Ca1-$O1^{ii}$ | 75.46(5) | $O3^{vi}$-Ca2-$Cl1^{ix}$ | 120.9(3) |
| $O1^{i}$-Ca1-O1 | 75.46(5) | $O3^{vii}$-Ca2-$Cl1^{ix}$ | 83.3(3) |
| $O1^{ii}$-Ca1-O1 | 75.46(5) | $O2^{viii}$-Ca2-$Cl1^{ix}$ | 146.54(2) |
| $O1^{i}$-Ca1-$O2^{iii}$ | 91.89(5) | $O3^{vi}$-Ca2-$O3^{xi}$ | 79.21(3) |
| $O1^{ii}$-Ca1-$O2^{iii}$ | 153.37(6) | $O3^{vii}$-Ca2-$O3^{xi}$ | 137.15(6) |
| O1-Ca1-$O2^{iii}$ | 124.57(6) | $O2^{viii}$-Ca2-$O3^{xi}$ | 74.56(6) |
| $O1^{i}$-Ca1-$O2^{iv}$ | 153.37(6) | $F1^{ix}$-Ca2-$O3^{xi}$ | 81.48(4) |
| $O1^{ii}$-Ca1-$O2^{iv}$ | 124.57(6) | $Cl1^{x}$-Ca2-$O3^{xi}$ | 72.23(1) |
| O1-Ca1-$O2^{iv}$ | 91.89(5) | $Cl1^{ix}$-Ca2-$O3^{xi}$ | 91.50(2) |
| $O2^{iii}$-Ca1-$O2^{iv}$ | 75.91(5) | $O3^{vi}$-Ca2-O3 | 137.15(6) |
| $O1^{i}$-Ca1-$O2^{v}$ | 124.57(6) | $O3^{vii}$-Ca2-O3 | 79.21(3) |
| $O1^{ii}$-Ca1-$O2^{v}$ | 91.89(5) | $O2^{viii}$-Ca2-O3 | 74.56(6) |
| O1-Ca1-$O2^{v}$ | 153.37(6) | $F1^{ix}$-Ca2-O3 | 81.48(4) |
| $O2^{iii}$-Ca1-$O2^{v}$ | 75.91(5) | $Cl1^{x}$-Ca2-O3 | 91.50(2) |
| $O2^{iv}$-Ca1-$O2^{v}$ | 75.91(5) | $Cl1^{ix}$-Ca2-O3 | 72.23(1) |
| $O1^{i}$-Ca1-$O3^{iii}$ | 85.58(5) | $O3^{xi}$-Ca2-O3 | 58.90(7) |
| $O1^{ii}$-Ca1-$O3^{iii}$ | 143.16(5) | $O3^{vi}$-Ca2-$O4^{ix}$ | 78(4) |
| O1-Ca1-$O3^{iii}$ | 69.26(5) | $O3^{vii}$-Ca2-$O4^{ix}$ | 126(4) |
| $O2^{iii}$-Ca1-$O3^{iii}$ | 55.91(5) | $O2^{viii}$-Ca2-$O4^{ix}$ | 143(3) |
| $O2^{iv}$-Ca1-$O3^{iii}$ | 67.94(5) | $O3^{xi}$-Ca2-$O4^{ix}$ | 69.8(2) |
| $O2^{v}$-Ca1-$O3^{iii}$ | 124.66(5) | O3-Ca2-$O4^{ix}$ | 94(2) |
| $O1^{i}$-Ca1-$O3^{v}$ | 69.26(5) | $O3^{vi}$-Ca2-$O4^{x}$ | 126(4) |
| $O1^{ii}$-Ca1-$O3^{v}$ | 85.58(5) | $O3^{vii}$-Ca2-$O4^{x}$ | 78(4) |
| O1-Ca1-$O3^{v}$ | 143.16(5) | $O2^{viii}$-Ca2-$O4^{x}$ | 143(3) |
| $O2^{iii}$-Ca1-$O3^{v}$ | 67.94(5) | $O3^{xi}$-Ca2-$O4^{x}$ | 94(2) |
| $O2^{iv}$-Ca1-$O3^{v}$ | 124.66(5) | O3-Ca2-$O4^{x}$ | 69.8(2) |
| $O2^{v}$-Ca1-$O3^{v}$ | 55.91(5) | $O3^{vi}$-Ca2-$O1^{xii}$ | 70.98(4) |
| $O3^{iii}$-Ca1-$O3^{v}$ | 117.041(2) | $O3^{vii}$-Ca2-$O1^{xii}$ | 70.98(4) |
| $O1^{i}$-Ca1-$O3^{iv}$ | 143.16(5) | $O2^{viii}$-Ca2-$O1^{xii}$ | 102.95(6) |
| $O1^{ii}$-Ca1-$O3^{iv}$ | 69.26(5) | $F1^{ix}$-Ca2-$O1^{xii}$ | 104.66(4) |
| O1-Ca1-$O3^{iv}$ | 85.58(5) | $Cl1^{x}$-Ca2-$O1^{xii}$ | 103.79(5) |
| $O2^{iii}$-Ca1-$O3^{iv}$ | 124.66(5) | $Cl1^{ix}$-Ca2-$O1^{xii}$ | 103.79(5) |
| $O2^{iv}$-Ca1-$O3^{iv}$ | 55.91(5) | $O3^{xi}$-Ca2-$O1^{xii}$ | 150.19(3) |
| $O2^{v}$-Ca1-$O3^{iv}$ | 67.94(5) | O3-Ca2-$O1^{xii}$ | 150.19(3) |
| $O3^{iii}$-Ca1-$O3^{iv}$ | 117.041(2) | $O4^{ix}$-Ca2-$O1^{xii}$ | 103.2(5) |
| $O3^{v}$-Ca1-$O3^{iv}$ | 117.041(2) | $O4^{x}$-Ca2-$O1^{xii}$ | 103.2(5) |
| $O3^{vi}$-Ca2-$O3^{vii}$ | 138.80(8) | O1-P1-O2 | 111.08(1) |
| $O3^{vi}$-Ca2-$O2^{viii}$ | 86.77(4) | O1-P1-O3 | 111.47(8) |
| $O3^{vii}$-Ca2-$O2^{viii}$ | 86.77(4) | O2-P1-O3 | 107.48(8) |
| $O3^{vi}$-Ca2-$F1^{ix}$ | 102.17(4) | O3-P1-O3 | 107.67(1) |
| $O3^{vii}$-Ca2-$F1^{ix}$ | 102.17(4) | O3-P1-$O3^{xi}$ | 107.68(1) |
| $O2^{viii}$-Ca2-$F1^{ix}$ | 152.39(5) | O3-P1-O1 | 111.46(7) |
| $O3^{vi}$-Ca2-$Cl1^{x}$ | 83.3(3) | $O3^{xi}$-P1-O1 | 111.46(7) |
| $O3^{vii}$-Ca2-$Cl1^{x}$ | 120.9(3) | O3-P1-O2 | 107.48(8) |
| $O2^{viii}$-Ca2-$Cl1^{x}$ | 146.54(2) | $O3^{xi}$-P1-O2 | 107.48(8) |

*Note:* Symmetry codes: (i) $1 - y, x - y, z$; (ii) $1 - x + y, 1 - x, z$; (iii) $y, - x + y, - z$; (iv) $1 - x, 1 - y, - z$; (v) $1 + x - y, x, - z$; (vi) $x - y, x, 0.5 + z$; (vii) $x - y, x, - z$; (viii) $- x + y, 1 - x, z$; (ix) $- 1 + x, y, z$; (x) $- 1 + x, y, 0.5 - z$; (xi) $x, y, 0.5 - z$; (xii) $- y, x - y, z$; (xiii) $1 - x, 1 - y, 0.5 + z$; (xiv) $- x + y, - x, z$; (xv) $1 - y, 1 + x - y, z$; (xvi) $1 + x, y, z$; (xvii) $1 - x + y, - x, z$; (xviii) $2 - x, - y, - 0.5 + z$; (xix) $2 - x, - y, - z$; (xx) $2 - x, - y, 1 - z$; (xxi) $2 - x, - y, 0.5 + z$.

visualized through the program MAX3D, which combines all diffraction frames and makes 3-D images of the reciprocal space. The program revealed the presence of spot-splitting and diffuse scattering consistent with incommensurate scattering occurring perpendicular to the $a^*c^*$ plane (Fig. 1).

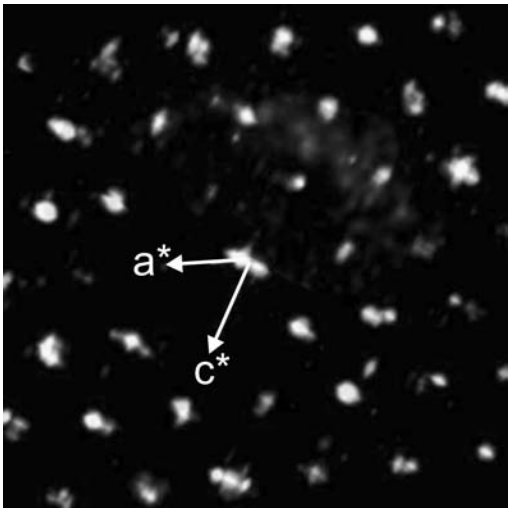


**FIGURE 1.** A snapshot of the single-crystal X-ray diffraction data using MAX3D. The splitting of the diffraction spots suggests incommensurate scattering perpendicular to the $a^*c^*$ plane.

## NMR spectroscopy

$^{31}$P Single-Pulse (SP) MAS NMR spectra reveal a complex lineshape for the synthesized apatite that appears to contain a peak at +2.9 ppm and a shoulder at +1.7 ppm (Fig. 2a). $^{31}$P{$^{19}$F} CP/MAS spectra collected at a variety of contact times (Figs. 2b–2c) are all essentially identical to the SP spectrum. The $^{31}$P{$^{1}$H} CP/MAS spectra (Fig. 2d) contain a broad asymmetric peak that resembles the shape of the $^{31}$P SP and $^{31}$P{$^{19}$F} CP/MAS spectra. The similarity of the SP and CP/MAS spectra indicate that the structure observed in these spectra does not arise from local variations in the distribution of F, Cl, and OH in the channels. For example, $^{31}$P{$^{19}$F} CP/MAS at short contact time would selectively enhance the signal from P near any F-rich clusters, but the data show no evidence for distinct spectral features at short (0.3 ms) contact time. The XRD results show only a single crystallographic P position. We tentatively attribute the structure in the $^{31}$P peak shape to a structural modulation that was also noted in the XRD data (Fig. 1). Effects of non-linear structural modulations on MAS NMR spectra are described by Phillips (2000).

The $^{19}$F SP MAS spectrum of the synthetic apatite sample shows a peak shape that appears to contain a peak at –103.3 ppm and a shoulder at –97.4 ppm (Fig. 3a). The peak at –103.3 ppm is similar to those previously reported for fluorapatites (Braun et al. 1995). This spectral profile also occurs in the spinning sidebands and did not vary with relaxation delays, indicating the F species represented by these peaks are contained in the same phase.

$^{19}$F{$^{35}$Cl} TRAPDOR NMR data were collected to investigate the connectivity of the $^{19}$F and $^{35}$Cl spins in the apatite channels. Figures 3b–3d shows the results obtained using an echo delay of 12 rotor cycles (750 µs). The $^{19}$F spin-echo spectrum ($S_0$; Fig. 3b) shows all of the $^{19}$F in the sample and closely resembles the SP spectrum, with two features seen at –97.4 ppm and –103.3 ppm and spinning sidebands. The TRAPDOR NMR experiment reduces the signal intensity for F located near the $^{35}$Cl spins by irradiation at the $^{35}$Cl frequency during the $^{19}$F spin-echo, which recouples the dipolar interactions between the $^{19}$F and $^{35}$Cl spins. The results ($S$; Fig. 3c) show a significant TRAPDOR effect, $(1 - S/S_0) \approx 0.5$ for these experimental conditions, indicating close F-Cl spatial proximity. The TRAPDOR difference spectrum ($S_0 - S$; Fig. 3d) contains signal only from $^{19}$F species that are associated with the $^{35}$Cl spins in the sample and shows no change in the spectral profile compared to the spin-echo and SP spectra. $^{19}$F{$^{35}$Cl}. TRAPDOR data collected at irradiation periods ($\tau$) from 0.125 to 5 ms show that the TRAPDOR fraction, $(S_0 - S)/S_0$, rapidly approaches 0.94 (Fig. 4a). This value is consistent with a well-ordered F/Cl distribution, in which 6% of the F should have

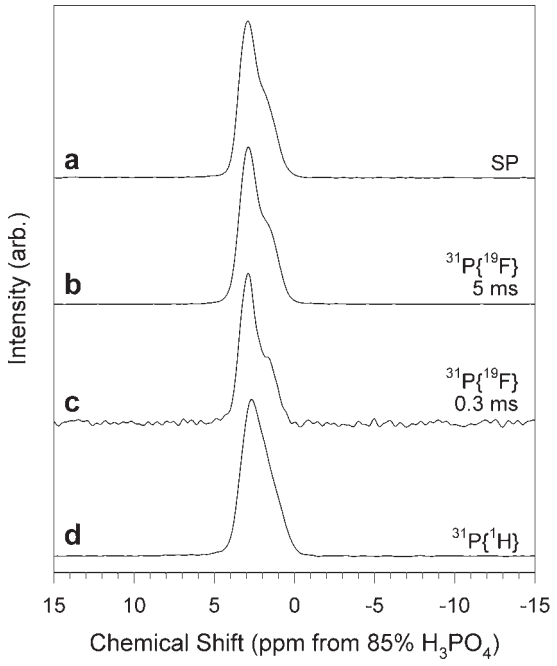


**FIGURE 2.** $^{31}$P MAS NMR spectra of the synthesized apatite sample. (**a**) $^{31}$P SP spectrum (SP) at a pulse delay of 120 s. (**b**) $^{31}$P{$^{19}$F} CP/MAS spectrum at a contact time of 5 ms and a pulse delay of 60 s. (**c**) $^{31}$P{$^{19}$F} CP/MAS spectrum at a contact time of 0.3 ms and a pulse delay of 60 s. (**d**) $^{31}$P{$^{1}$H} CP/MAS spectrum at a contact time of 5 ms and pulse delay of 10 s.

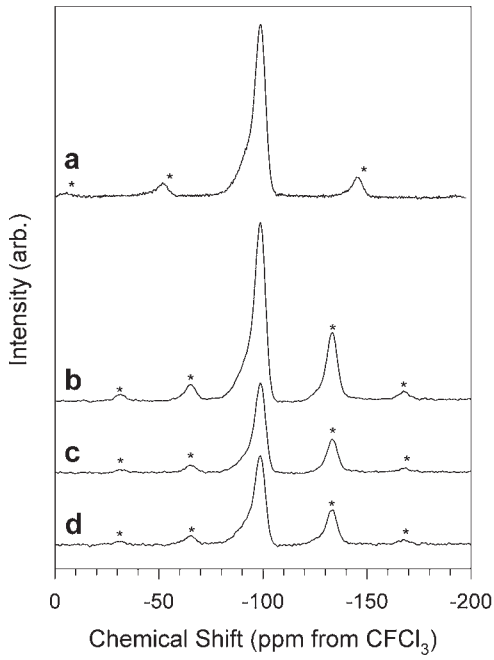


**FIGURE 3.** $^{19}$F NMR spectra of the synthesized apatite sample (**a**) $^{19}$F SP MAS NMR spectrum collected at a spinning rate of 24 kHz and pulse delay of 200 s. (**b**–**d**) $^{19}$F{$^{35}$Cl} TRAPDOR spectral set collected at 12 rotor-cycle echo delay using a spinning rate of 16 kHz and a pulse delay of 100 s. (**b**) $^{19}$F echo control spectrum, $S_0$. (**c**) $^{19}$F-$^{35}$Cl TRAPDOR spectrum, $S$. (**d**) Difference spectrum, $S_0 - S$. Spectra **b**–**d** are scaled to reflect the absolute intensities. Asterisks denote spinning sidebands.

two $^{37}$Cl neighbors (24.47% natural abundance). These results indicate that all of the F atoms are closely associated with Cl atoms in this sample and that the asymmetric spectral profile does not arise from variations in the local Cl, F distribution.

$^{35}$Cl SP MAS NMR spectra (not shown) were taken to derive information needed for the $^{19}$F{$^{35}$Cl} TRAPDOR NMR experiments. The $^{35}$Cl NMR signal is easily observed and is characterized by a second-order quadrupolar lineshape with a chemical shift of about +115 ppm and a quadrupolar coupling constant of $C_Q$ = 1.6 MHz. This value is somewhat larger than a previously reported measurement for chlorapatite, $C_Q$ = 0.8 MHz (Bryce and Sward 2006).

Simulations using the SIMPSON software package (Bak et al. 2000) were also preformed to analyze the variation in the TRAPDOR effect with $^{19}$F-$^{35}$Cl internuclear distance. We used the internuclear distances of 2.62 and 5.31 Å derived from X-ray diffraction results corresponding to isolated F-Cl spin pairs occupying adjacent column positions and those separated by two intracolumn distances (Table 5). The simulations indicate that at a separation of 2.62 Å the TRAPDOR fraction, $(S_0 - S)/S_0$, reaches 0.90 by 5 ms; a separation of 5.31 Å yields a TRAPDOR fraction less than 0.10 at 5 ms (Fig. 4b). Thus, $^{19}$F{$^{35}$Cl} TRAPDOR spectra at $\tau$ = 5ms would contain <10% signal from any F further than one column spacing from Cl. No observable TRAPDOR fraction was found for simulations run at distances comparable to those for inter-channel separation (ca. 9 Å; not shown). These results correspond well to the TRAPDOR fractions we derived experimentally, which show a TRAPDOR fraction of 0.94 at 5 ms (Fig. 4a). A more rapid increase in the TRAPDOR fraction is observed experimentally because the simulations used a single $^{19}$F-$^{35}$Cl spin pair, whereas 57% of the F in the apatite should have two $^{35}$Cl neighbors (75.5% natural abundance). The key point is that the observed TRAPDOR effect is consistent with neighboring F and Cl within the channels as indicated by the XRD data, but could not arise from interactions of F and Cl located in adjacent anion channels. These observations are also consistent with F,Cl ordering in the channels, which would yield a maximum TRAPDOR fraction of about 0.94 considering that 6% of the F should have two $^{37}$Cl intracolumn neighbors (24.47% natural abundance). The $^{37}$Cl atoms do not contribute to the $^{19}$F{$^{35}$Cl} TRAPDOR effect. If F-rich clusters were present within the channels, the TRAPDOR fraction would be expected to be less than 0.94 because of the F atoms positioned farther than 5 Å from Cl (Fig. 4b). These TRAPDOR data indicate that there is no appreciable population of F atoms farther than 2.62 Å from any Cl atom.

To determine whether the synthetic apatite contained a significant hydroxyl component, $^{1}$H NMR spectra were obtained. The $^{1}$H SP MAS spectra of the synthetic apatite can be described by a broad resonance at +6.6 ppm, and three sharp resonances at +3.2, +1.9, and +1.1 ppm (Fig. 5a). We do not observe any peaks in the range that would be expected for a pure hydroxylapatite, +0.2 ppm (Yesinowski and Eckert 1987). The peak at +6.6 ppm exhibits a broad spinning sideband manifold (not shown in Fig.

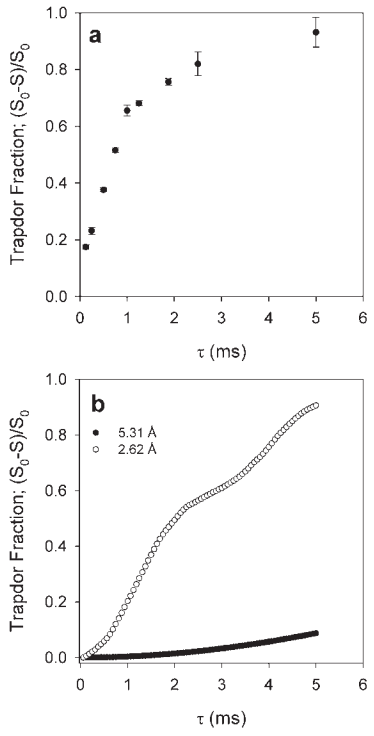


**FIGURE 4.** (**a**) Experimentally measured TRAPDOR fraction, $(S_0 - S)/S_0$, as a function of the irradiation period (τ) for the synthetic apatite. (**b**) Calculated TRAPDOR fraction, $(S_0 - S)/S_0$, as a function of irradiation period (τ) using F-Cl distances calculated from the X-ray diffraction study for the synthetic apatite corresponding to adjacent column positions (2.62 Å, open symbols) and a those separated by two column positions (5.31 Å, closed symbols).

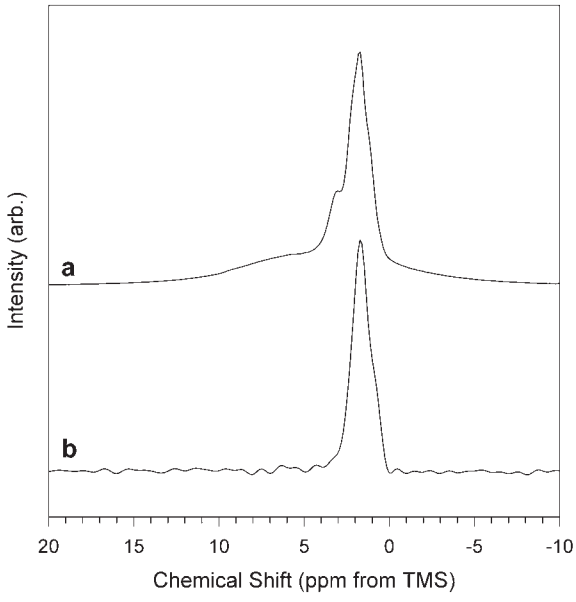


**FIGURE 5.** $^{1}$H MAS NMR spectra of the FClAp sample (**a**) $^{1}$H SP spectrum collected at a 10 s pulse delay and 15 kHz spinning rate. (**b**) Indirectly detected $^{1}$H spectrum from $^{31}$P{$^{1}$H} HetCor NMR spectrum of FClAp (slice taken at $^{31}$P chemical shift of +2.9 ppm). A total of 128 hypercomplex increments in t1 were collected for 64 counts each at a spinning rate of 10 kHz, a pulse delay of 10 s, and a contact time of 5 ms.

5a) that indicates it arises from rigid water molecules. The peaks at +1.9 and +1.1 ppm correspond closely to chemical shifts observed by Yesinowski and Eckert (1987) for a series of mixed fluor-hydroxylapatites. These authors assigned peaks in the range of +1.5 to +1.6 ppm to $OH^{-}\cdots F^{-}\cdots OH^{-}$ or $OH^{-}\cdots F^{-}\cdots F^{-}$ configuration and peaks in the range of +1.2 to +1.4 ppm to $OH^{-}\cdots F^{-}\cdots HO^{-}$. $^{31}$P{$^{1}$H} HetCor NMR spectra of this sample were collected at a variety of contact times, all of which show only the peaks at +1.9 and +1.1 ppm in the $^{31}$P-detected $^{1}$H dimension (Fig. 5b). This result indicates that only the H atoms corresponding to these peaks are associated with the P in the apatite. Assignment of the peaks at +3.2 and +6.6 ppm is uncertain but the HetCor data show that they are not contained in the apatite. The $^{1}$H peaks at +3.2 and +6.6 ppm in this sample also exhibit spin lattice relaxation times ($T_1$; observed as variations in relative intensity difference with pulse delay) that differ from those of the peaks at +1.9 and +1.1 ppm. This is consistent with the occurrence of these H atoms in a separate phase. These observations suggest that the peaks at +6.6 and +3.8 ppm, which represent about 67% of the H in the sample, arise from unknown impurity phases in the sample, possibly unreacted $CaCl_2$.

## DISCUSSION

X-ray powder diffraction and EPMA analysis of the synthesized apatite crystals verified chemical homogeneity on the sample scale and the single-crystal scale, respectively (compositional range is $F_{0.51–0.48}Cl_{0.38–0.36}OH_{0.14–0.12}$); however, neither of the techniques could verify the presence or absence of fluor-rich and chlor-rich domains in the apatite crystals. Absence of such domains was verified by $^{19}$F{$^{35}$Cl} TRAPDOR NMR experiments, which show that F and Cl atoms must be within about 3 Å of each other to describe the observed TRAPDOR effect. The anion position refinements indicate Cl···F inter-column distances of 2.62 Å, consistent with the $^{19}$F{$^{35}$Cl} TRAPDOR NMR experiments.

The synthesized apatite was carefully indexed as hexagonal with space group $P6_3/m$, however the presence of incommensurate scattering suggests that the apatite may have some localized ordering with respect to anionic sequences within the hexagonal columns. This ordering was not extensive enough to induce overall monoclinic symmetry, but the presence of short-range monoclinic domains within the overall hexagonal average structure would be in agreement with the suggestions of Hughes and Rakovan (2002). Additionally, complex lineshapes in the $^{31}$P and $^{19}$F MAS NMR spectra were observed. $^{31}$P{$^{19}$F} CP/MAS NMR experiments conducted at short contact times led to the conclusion that F-rich clusters are absent within the apatite channels and such clusters, therefore, cannot account for the complex lineshape in the $^{31}$P MAS NMR spectra. We attribute the complex lineshapes in the $^{31}$P and $^{19}$F MAS NMR spectra to

the presence of the incommensurate structural modulations. The $^{31}P\{^{19}F\}$ CP/MAS NMR results provide additional evidence for anionic mixing within the apatite channels because they further verify that the channels are mixed with respect to fluorine.

The apatite synthesized for this study was not $OH^-$-free (as determined both by difference using EPMA data, and by $^{31}P\{^{1}H\}$ CP/MAS and HetCor NMR). Therefore, the stability of truly binary F-Cl apatite cannot be directly inferred from this work. However, these results indicate the possible stability of binary ($OH^-$-free) fluor-chlorapatite and warrant further concerted synthesis efforts.

## Acknowledgments

The authors thank Yu-Sheng Chen at ChemMatCARS, APS, for his assistance with single-crystal X-ray diffraction. ChemMatCARS Sector 15 is principally supported by the National Science Foundation/Department of Energy under grant CHE-0087817. The Advanced Photon Source is supported by the U.S. Department of Energy, Basic Energy Sciences, Office of Science, under contract no. W-31-109-Eng-38. The MAX3D image was provided by J.F. Britten at the Department of Chemistry, McMaster University. This work was partially supported by NASA grant NNG04GM79G awarded to Hanna Nekvasil. Harris Mason was supported by the NSF EMSI program, CHE-0221934. NMR instrumentation was purchased by a grant from the NSF, CHE-0321001, and partially supported by EAR-0310200. Hyunsoo Park is grateful for support from NSF-DMR 0452444 and EAR-0510501 to John B. Parise. We also thank John M. Hughes, Michael Fechtelkord, and Richard Thompson for insightful and thorough reviews of this paper, and we thank Michael Fechtelkord and George Lager for the editorial handling of this paper.

## References cited

Bak, M., Rasmussen, J.T., and Nielsen, N.C. (2000) SIMPSON: A general simulation program for solid-state NMR spectroscopy. Journal of Magnetic Resonance, 147, 296–330.

Boudreau, A.E., Love, C., and Prendergast, M.D. (1995) Halogen geochemistry of the Great Dyke, Zimbabwe. Contributions to Mineralogy and Petrology, 122, 289–300.

Braun, M., Hartmann, P., and Jana, C. (1995) $^{19}F$ and $^{31}P$ NMR-Spectroscopy of calcium apatites. Journal of Materials Science: Materials in Medicine, 6, 150–154.

Brese, N.E. and O'Keeffe, M. (1991) Bond-valence parameters for solids. Acta Crystallographica Section B: Structural Science, 47, 192–197.

Bryce, D.L. and Sward, G.D. (2006) Solid-state NMR spectroscopy of the quadrupolar halogens: chlorine-35/37, bromine-79/81, and iodine-127. Magnetic Resonance in Chemistry, 44, 409–450.

Bunch, T. and Reid, A. (1975) The Nakhlites, part 1. Petrography and mineral chemistry. Meteoritics 10, 303–315.

Grey, C.P. and Vega, A.J. (1995) Determination of the quadrupole coupling-constant of the invisible aluminum spins in zeolite Hy with $^{1}H/^{27}Al$ TRAPDOR NMR. Journal of the American Chemical Society, 117, 8232–8242.

Hughes, J.M. and Rakovan, J. (2002) The crystal structure of apatite, $Ca_5(PO_4)_3(F,OH,Cl)$. Phosphates: Geochemical, Geobiological, and Materials Importance, 48, p. 1–12.

Hughes, J.M., Cameron, M., and Crowley, K.D. (1989) Structural variations in natural F, OH, and Cl apatites. American Mineralogist, 74, 870–876.

——— (1990) Crystal-structures of natural ternary apatites—solid-solution in the $Ca_5(PO_4)_3X$ (X= F, OH, Cl) system. American Mineralogist, 75, 295–304.

Jolliff, B.L., Haskin, L.A., Colson, R.O., and Wadhwa, M. (1993) Partitioning in REE-saturating minerals—theory, experiment, and modeling of whitlockite, apatite, and evolution of lunar residual magmas. Geochimica et Cosmochimica Acta, 57, 4069–4094.

McCubbin, F.M., Nekvasil, H., and Lindsley, D.H. (2006) Apatite as a key to evaluating the volatile budget of martian magmas: implications from the Chassigny meteorite, p. 1098. Proceedings of the Lunar and Planetary Science Conference XXXVII, Houston, Texas.

——— (2007) Late-stage volatile evolution in martian magmas: Inferences from maskelynite-hosted apatite of the Chassigny meteorite, p. 1347. Proceedings of the Lunar and Planetary Science Conference XXXVIII, Houston, Texas.

Pan, Y.M. and Fleet, M.E. (2002) Compositions of the apatite-group minerals: Substitution mechanisms and controlling factors. In M.L. Kohn, J. Rakovan, and J.M. Hughes, Eds., Phosphates—Geochemical, Geobiological, and Materials Importance, 48, p. 13–49. Reviews in Minerals and Geochemistry, Mineralogical Society of America, Chantilly, Virginia.

Phillips, B.L. (2000) NMR spectroscopy of phase transitions in minerals. In S.A.T. Redfern and M.A. Carpenter, Eds., Transformation Processes in Minerals, 39, p. 203–240. Reviews in Minerals and Geochemistry, Mineralogical Society America, Chantilly, Virginia.

Piccoli, P.M. and Candela, P.A. (2002) Apatite in igneous systems. In M.L. Kohn, J. Rakovan, and J.M. Hughes, Eds., Phosphates—Geochemical, Geobiological, and Materials Importance, 48, p. 255–292. Reviews in Minerals and Geochemistry, Mineralogical Society of America, Chantilly, Virginia.

SAINT (2002) Siemens Analytical INTegration software. Bruker-AXS. Madison, Wisconsin.

Sheldrick, G.M. (2000) SHELXTL, 6.10. Bruker-AXS. Madison, Wisconsin.

——— (2001) SADABS, a program for the Siemens area detector absorption. Bruker-AXS. Madison, Wisconsin.

SMART (2001) Siemens Molecular Analysis Research Tool. Bruker-AXS. Madison, Wisconsin.

Stormer, J.C., Pierson, M.L., and Tacker, R.C. (1993) Variation of F-X-ray and Cl-X-ray intensity due to anisotropic diffusion in apatite during electron-microprobe analysis. American Mineralogist, 78, 641–648.

Sudarsanan, K. and Young, R.A. (1969) Significant precision in crystal structural details. Holly Springs hydroxyapatite. Acta Crystallographica Section B: Structural Crystallography and Crystal Chemistry, B25, 1534–1543.

Tacker, R.C. and Stormer, J.C. (1989) A thermodynamic model for apatite solid-solutions, applicable to high-temperature geologic problems. American Mineralogist, 74, 877–888.

Taylor, L.A., Patchen, A., Mayne, R.G., and Taylor, D.H. (2004) The most reduced rock from the moon, Apollo 14 basalt 14053: Its unique features and their origin. American Mineralogist, 89, 1617–1624.

White, T.J. and Dong, Z.L. (2003) Structural derivation and crystal chemistry of apatites. Acta Crystallographica Section B: Structural Science, 59, 1–16.

Yesinowski, J.P. and Eckert, H. (1987) Hydrogen environments in calcium phosphates $^{1}H$ MAS NMR at high spinning speeds. Journal of the American Chemical Society, 109, 6274–6282.

Manuscript received January 9, 2007
Manuscript accepted September 12, 2007
Manuscript handled by Michael Fechtelkord